separations

MDPI

Article

Photocatalytic Degradation of Levofloxacin and Inactivation of Enterococci Levofloxacin-Resistant Bacteria Using Pure Rare-Earth Oxides

Lorenzo Saviano [1], Antonietta Mancuso [2,*], Alice Cardito [3], Olga Sacco [3,*], Vincenzo Vaiano [2], Maurizio Carotenuto [3], Giovanni Libralato [1] and Giusy Lofrano [4]

[1] Department of Biology, University of Naples Federico II, 80126 Naples, Italy; lorenzo.saviano@unina.it (L.S.); giovanni.libralato@unina.it (G.L.)
[2] Department of Industrial Engineering, University of Salerno, 84084 Fisciano, Italy; vvaiano@unisa.it
[3] Department of Chemistry and Biology "Adolfo Zambelli", University of Salerno, 84084 Fisciano, Italy; acardito@unisa.it (A.C.); mcarotenuto@unisa.it (M.C.)
[4] Department of Movement, Human and Health Sciences, University of Rome "Foro Italico", 00135 Rome, Italy; glofrano@unisa.it
* Correspondence: anmancuso@unisa.it (A.M.); osacco@unisa.it (O.S.)

Abstract: In this study, La_2O_3 and CeO_2 nanopowders were prepared using a simple and cost-effective precipitation method. Wide-angle X-ray diffraction (WAXD), UV-Visible reflectance diffuses (UV-Vis DRS), Raman spectroscopy, and specific surface area were used to characterize the photocatalysts, evidencing that the used preparation method was effective in the generation of crystalline CeO_2 and La_2O_3. In particular, WAXD results showed that the average crystallite size of the achieved La_2O_3 and CeO_2 samples were about 22 nm and 28 nm, respectively. The photocatalytic performances of the prepared catalysts were investigated in the degradation of levofloxacin (LEV) and the inactivation of a waterborne pathogen levofloxacin resistant (*Enterococcus faecalis* ATCC 29212) by using a photoreactor equipped with a solar simulator (SS). After 120 min, the CeO_2 and La_2O_3 photocatalytic treatments allowed us to achieve between 75% and 83% of levofloxacin removal, respectively. A complete removal of 10^6 CFU/mL *Enterococcus faecalis* ATCC 29212 was achieved after 5 and 60 min of La_2O_3 and CeO_2 photocatalytic processes, respectively.

Keywords: rare earth oxide; levofloxacin; bacteria inactivation; photocatalysis; solar light

Citation: Saviano, L.; Mancuso, A.; Cardito, A.; Sacco, O.; Vaiano, V.; Carotenuto, M.; Libralato, G.; Lofrano, G. Photocatalytic Degradation of Levofloxacin and Inactivation of Enterococci Levofloxacin-Resistant Bacteria Using Pure Rare-Earth Oxides. *Separations* **2024**, *11*, 272. https://doi.org/10.3390/separations11090272

Academic Editor: Grzegorz Boczkaj

Received: 5 July 2024
Revised: 15 September 2024
Accepted: 16 September 2024
Published: 18 September 2024

1. Introduction

To avert the global water crisis and the shortage of natural resources, the development of sustainable and innovative strategies to treat and reuse wastewater is urgently required. Wastewater contains a wide category of contaminants, both organic and inorganic, including pathogens which could be released into the environment, threatening human health directly or indirectly when they are not properly removed. Among several contaminants of emerging concern (CECs), the occurrence of antibiotics in wastewater is gaining growing attention due to the limit of conventional wastewater treatment to remove such kinds of compounds [1].The chronic release of antibiotics into receiving water bodies leads to direct and indirect effects in human beings by bioaccumulation and antibiotic resistance. Recently, multiple genetic and genomic studies proved that wastewater treatment plants are sinks of resistant genes and organisms [2,3], increasing the spread of resistant strains into the environment. *Enterococcus faecalis* is a familiar urinary tract infection (UTI) pathogen of bacterial origin, recently recognized as an emerging concern due to its increasing resistance to antimicrobials, mainly vancomycin and levofloxacin [4]. To date, several conventional disinfection methods have been used to remove pathogens in wastewater, the most common being chlorination [5]. However, several potential ecological risks have been associated with chlorine, including the production of toxic disinfection

byproducts (DBPs) [6]. Thus, research is pushing towards alternative treatments, including advanced oxidation processes (AOPs), which present excellent capability to degrade CECs and to inactivate waterborne pathogens through highly reactive oxidizing species [7–9]. Heterogeneous photocatalysis, with the application of semiconductor materials as photocatalysts, is one of the most prominent approaches to remove several contaminants of emerging concern, including waterborne pathogens from wastewater [10–12]. Titanium oxide (TiO_2) and zinc oxide (ZnO) are considered to be excellent photocatalysts due to their high stability higher efficiency, low cost, easy availability, lower toxicity, eco-friendliness, and highly oxidizing photo-generated holes [13]. However, there are several drawbacks to utilizing metal oxide for photocatalytic degradation, such as incomplete mineralization and a wide band gap [14], which limit their photocatalytic activity. Over the last few years, substantial efforts have been made towards study of extremely effective photocatalysts for the oxidative decomposition of organic pollutants to end products, such as carbon dioxide (CO_2) and water (H_2O) [15]. Specifically, rare earth (REEs) metal oxides have generated great interest as a practical way to hike the efficiency of photocatalytic processes. Studies focused on the use of lanthanides have demonstrated an improvement in wastewater treatments, as their use can produce, on average, 30% less sludge compared to other alternatives such as iron and aluminum [16]. The use of REEs, such as lanthanum (La), cerium (Ce), gadolinium, etc., could represent an alternative for reducing wastelands generated by sludge [16] and could improve the removal of organic pollutants by enhancing photocatalytic activity [17]. Specifically, rare earth semiconductors have gained great attention for their tunable band alignments, modulated atomic configurations, singular electronic states, and efficient optoelectric properties. For example, the particular electronic band structure of La_2O_3 allows for the formation of complexes with various Lewis bases, assuring an improvement of optical collection, which consequently promotes photocatalytic efficiency and stability [18,19]. On the other hand, the presence of crystal defects in the CeO_2 lattice due to the high amount of oxygen vacancies prevents the recombination of electron-hole ions, thus improving the photocatalytic degradation performance. Various physical and chemical processes can be used to produce REE nanoparticles; thermal decomposition, mechanical milling, and fame spray are examples of physical processes, [20,21] whereas hydrothermal, sol–gel, combustion methods, microemulsion, chemical co-precipitation, and vapor deposition are chemical processes [22]. Among the synthetic methods, the chemical precipitation process has several benefits, including low cost and the absence of hazardous substances [23]. In this work, lanthanum oxide (La_2O_3) and cerium oxide (CeO_2) were synthesized using a simple precipitation method for the photocatalytic degradation of levofloxacin (LEV) and the inactivation of a levofloxacin Enterococcus-resistant strain (*Enterococcus faecalis* ATCC 29212). To the best of our knowledge, this is the first study investigating the LEV degradation and the inactivation of a levofloxacin Enterococcus-resistant strain using pristine rare earths oxides.

2. Materials and Methods

The precursors for the design of the REE catalyst were cerium nitrate hexahydrate ($Ce(NO_3)_3{\cdot}6H_2O$, 99%; Sigma Aldrich) and lanthanum nitrate hexahydrate ($La(NO_3)_3{\cdot}6H_2O$, 99.9%; Sigma Aldrich). For the preparation of the Enterococci-selective agars, Tryptic Soy Broth (TSB, Difco, Becton-Dickenson Labs) and Slanetz and Bartley agar without TTC (Biolife, Monza, Italy) were used. Levofloxacin (98.0%) was purchased from Sigma Aldrich (Milan, Italy). All chemicals were analytical grade and were used as received without further purification. Deionized water was used throughout the experiments.

2.1. Catalysts Preparation Procedure

The precipitation method was used to synthesized single cerium and lanthanum oxide nanopowders (CeO_2, La_2O_3) (Figure 1) [24]. $Ce(NO_3)_3{\cdot}6H_2O$ or $La(NO_3)_3{\cdot}6H_2O$ were dissolved in Milli Q water up to the point where they reached a concentration of 0.2 M for each salt. Then, to the obtained solutions were added dropwise ammonium solution up

to pHs 8–8.5. The stirring was continued for 15 min after the completion of precipitation. The obtained colloidal solutions were washed with Milli Q water followed by four cycles of centrifugation at a speed of 3000 rpm (for 15 min). The resultant products were then dried in an oven at 110 °C for 8 h and crushed to powders. The oven-dried precursors were calcined at 850 °C for 2 h in air atmosphere to obtain CeO_2 and La_2O_3 nanopowders.

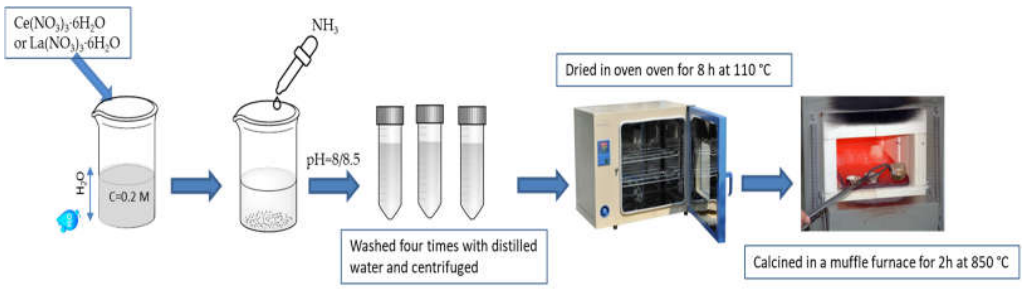

Figure 1. Schematic flow chart for the preparation of La_2O_3 andCeO_2 nanopowders.

2.2. Characterization Techniques

An automatic Bruker D8 Advance diffractometer (Billerica, MA, USA) with reflection geometry and nickel-filtered Cu-Kα radiation was used to obtain the wide-angle X-ray diffraction (WAXD) patterns. The lattice parameter values were determined using the following equations for the CeO_2 cubic structure (Equation (1)) and for the La_2O_3 hexagonal structure (Equation (2)), respectively:

$$\frac{1}{d_{hkl}^2} = \frac{\left(h^2 + k^2 + l^2\right)}{a^2} \quad (1)$$

$$\frac{1}{d_{hkl}^2} = \frac{4}{3}\frac{\left(h^2 + k^2 + hk\right)}{a^2} + \frac{l^2}{c^2} \quad (2)$$

where the value of d_{hkl} for a WAXD peak was determined using Bragg's law (Equation (3)):

$$2d_{hkl}sin\theta = \lambda \quad (3)$$

h, k, and l are the crystal plane indices, d_{hkl} is the spacing corresponding to the crystal plane (h k l), while a and c are the lattice parameters (for pure hexagonal phase of La_2O_3: $a = b \neq c$, $\alpha = \beta = 90°$ and $\gamma = 120°$; for pure cubic fluorite structure of CeO_2: $a = b = c$, $\alpha = \beta = \gamma = 90°$). To determine the lattice parameters' values, all of the planes for the hexagonal phase of La_2O_3 and for the cubic fluorite structure of CeO_2 were considered. The average crystallite size of CeO_2 and La_2O_3 were calculated using the Scherrer equation [25] (Equation (4)):

$$D = \frac{K\lambda}{\beta cos\theta} \quad (4)$$

where D is the average crystallite size (nm), K is the particle shape factor and taken as 0.89, λ is the X-ray wavelength corresponding to the Cu-Kα irradiation (1.5418 Å), β is the full width at half maximum (FWHM) of the diffraction peaks (radiant), and θ is the angle of Bragg diffraction [26]. The diffuse ultraviolet–visible reflectance (UV-Vis DRS) spectra of the samples, recorded with an RSA-PE-20 reflectance spectroscopy accessory (Labsphere Inc., North Sutton, NH, USA), were obtained using a Perkin Elmer Lambda 35 spectrophotometer (Waltham, MA, USA). The reflectance data were reported as the F(R∞) values, from Kubelka–Munk theory, versus wavelength. To estimate the indirect (Eg_i) and direct (Eg_d) band gap energies of the samples, $[F(R\infty) \times h\nu]^{1/2}$ versus photon energy ($h\nu$) and $[F(R\infty) \times h\nu]^2$ versus photon energy ($h\nu$) were calculated. From the intersection of the straight line with the x-axis, the Eg_i and Eg_d values of the photocatalysts were determined. Raman spectra were obtained using a Dispersive MicroRaman spectrometer

(Invia, Renishaw, Wotton-under-Edge, UK) using a laser with a radiation emission with a wavelength equal to 514 nm in the range of 100–1600 cm^{-1}. Fourier-transform infrared (FTIR) spectra were obtained with an FTIR (BRUKER Vertex70, Bruker, Karlsruhe, Germany) spectrometer equipped with a deuterated triglycine sulfate (DTGS) detector and a KBr beam splitter using KBr pellets. The spectra were obtained at a resolution of 2.0 cm^{-1} in the range of 400–4000 cm^{-1}. The BET specific surface area (S_{BET}) of photocatalysts were measured using dynamic N_2 adsorption measurements at −196 °C using the Sorptometer KELVIN 1042 instrument (Milano, Italy). The pore volume and mean pore radius were obtained by using a Nova Quantachrome 4200 e Instrument analyzer (Rome, Italy), applying the Barrett–Joyner–Halenda (BJH) method. Before the analysis, the samples were pretreated in He flow at 150 °C for 0.5 h.

2.3. Experimental Set-Up for Photocatalytic Tests

All of the photocatalytic tests were carried out in a jacketed custom-made photoreactor. The reactor consisted of a 100 mL cylindrical pyrex glass reactor vessel equipped with solar simulator (SS) (Xenon lamp) that provides illumination approximating natural sunlight (light power of 250 W/m^2, with a spectral wavelength range of 320–430 nm). The UV-A part of the solar spectrum is responsible for the activation of REE nanopowders in photocatalytic processes. The temperature was kept constant at 25 °C by circulating the cooling water continuously into the modified double-hinge photoreactor. Furthermore, the solutions were kept in constant magnetic mixing during the execution of the photocatalytic oxidation experiments (60 min dark + 180 min light for E. faecalis inactivation, 60 min dark + 120 min light for LEV removal). The photocatalytic tests were carried out by adding 0.5 g/L of photocatalysts (CeO_2 or La_2O_3) to a solution of the selected target, starting from an initial concentration of 10^6 CFU/mL for E. faecalis ATCC 29212 and 1 mg/L for LEV. The stirred mixture was left for 60 min in the dark to establish an equilibrium of adsorption between drug/bacteria and the catalyst. At defined time intervals (dark: 0, 5, 10, 15, 30, 60, 120, and 180 min), aliquots were sampled and centrifuged at 3000 rpm for 20 min.

In the case of the photocatalytic tests with LEV, a phosphate buffer with sodium dihydrogen phosphate/disodium hydrogen phosphate (NaH_2PO_4/Na_2HPO_4) was used to keep the pH constant at 7.00. For LEV detection, MeOH:10 mM CH_3COONH_4 (70:30 *v/v*) mixture was used for the mobile phase in the HPLC column, flowing at 1 mL/min through a Luna Phenomenex® C18 (250 4.6 mm; 5 m) column. Per run, a volume of 20 µL of the sample was injected and disclosed with a UV detector set at 295 nm.

2.4. Bacterial Count and Inactivation Test

LEV resistance phenotypes were tested using the Kirby–Bauer method according to standard recommendations [27]. The test allowed for the selection of the *Enterococcus faecalis* ATCC 29212 strain as resistant to levofloxacin. Briefly, the colonies, before the treatment, were transferred to appropriate culture broth for growing. Bacterial strains were grown to the exponential phase in Tryptic Soy Broth at 37 °C overnight. After 24 h, via spectrophotometric method at 590 nm, the density was adjusted to obtain a suspension of 0.5 McFarland (standard turbidity), corresponding approximately to 1–2 × 10^8 CFU/mL suspension. The inactivation experiment was conducted by spiking an aliquot of bacterial suspension with an initial density of 10^8 CFU/mL to the reaction solution, already added with the catalyst, in order to dilute it up to a concentration of 10^6 CFU/mL. The stirred mixture was then sampled after 60 min in the dark and then at time intervals of 0, 5, 10, 15, 30, 60, and 180 min. Subsequently, through the technique for inclusion of the inoculum in a solidifiable substrate ("Pour Plate"), the sample to be analyzed was inoculated into an empty sterile 90 mm Petri dish, then, adding the agarized substrate (12–15 mL), was kept in fusion at 45–46 °C. For this procedure, a selective medium for the isolation and enumeration of fecal streptococci (Slanetz and Bartley agar) was used. The inactivation of total (initial concentration 1.0 × 10^6 CFU/mL) Enterococci was evaluated after 24 h of incubation on this substrate. Bacterial count was performed in triplicate.

3. Results

3.1. Photocatalytic Materials Characterization

WAXD patterns of La_2O_3 and CeO_2 are shown in Figure 2.

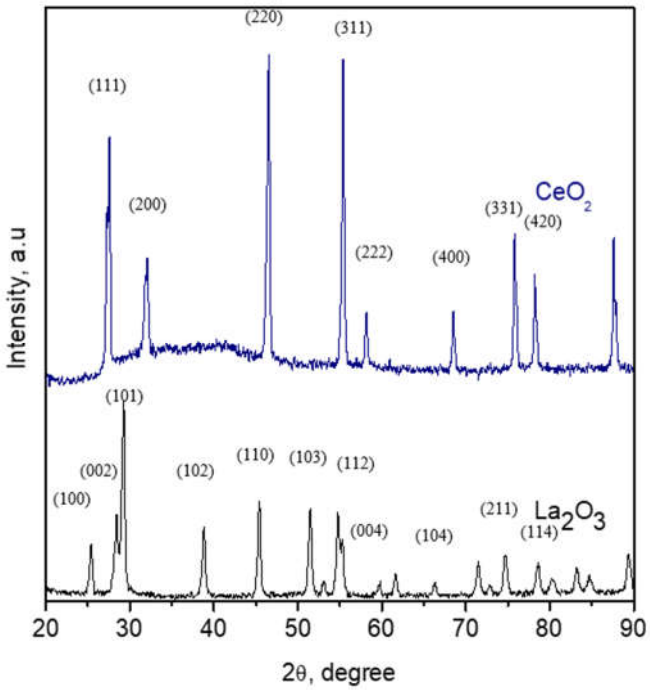

Figure 2. WAXD patterns of La_2O_3 and CeO_2 photocatalysts.

The main diffraction peaks for La_2O_3 at 2θ equal to 25.42°, 28.42°, 29.26°, 38.87°, 45.40°, 51.49°, 54.77°, 59.81°, 66.00°, 74.74°, and 78.60°, which refer to the crystalline planes (100), (002), (101), (102), (110), (103), (112), (004), (104), (211), and (114), respectively, are detectable. All of these signals are indicative of a hexagonal crystalline and correspond to the ICDD Card No. 01–083-1349 [26,28,29]. The diffraction peaks at 27.58°, 32.09°, 46.54°, 55.40°, 58.17°, 68.53°, 75.83°, and 78.22° are typical of CeO_2 cubic fluorite, and all diffraction signals are referred to (111), (200), (220), (311), (222), (400), (331), and (420) crystalline planes according to ICDD Card No (00-004-0593) [30,31]. Table 1 reports the average crystallite size, the cell parameters, the specific surface area evaluated using the BET method (S_{BET}), the direct energy of band gap (Eg_d), and the indirect energy of band gap (Eg_i) for the two oxides. The lattice parameter for CeO_2 is about 5.51 Å (Table 1) [32]. The average crystallite size of the CeO_2 is about 28 nm, in agreement with the literature, in which the CeO_2 sample prepared with the co-precipitation method reported a similar value of crystallite size of 20 nm [30]. On the other hand, the average crystallite size of La_2O_3 is equal to 22 nm, a value lower than that reported in the literature (41 nm). *a* and *c* lattice parameters for La_2O_3 are about 4.04 Å and 6.17 Å, respectively (Table 1). The S_{BET} value of La_2O_3 is 12 $m^2\ g^{-1}$ [33], while CeO_2 exhibits a very low S_{BET} value of about 2.4 $m^2\ g^{-1}$ [34].

Table 1. Crystallite size, lattice parameter, specific surface area (S_{BET}), direct band gap (Eg_d), and indirect band gap (Eg_i) of the samples.

Sample	D, nm	Lattice Parameters, A°		S_{BET}, $m^2\ g^{-1}$	Eg_d, eV	Eg_i, eV
		a = b	c			
La_2O_3	22 ± 5	4.04 ± 0.05	6.17 ± 0.04	12	5.46	5.32
CeO_2	28 ± 5	5.51 ± 0.05	–	2.4	2.81	2.59

The evaluation of band gap energy (Figure 3) showed that the Eg_i and Eg_d values of the La_2O_3 sample are 5.32 eV and 5.46 eV (Table 1), respectively. On the other hand, CeO_2 sample exhibits lower Eg_i and Eg_d values, equal to 2.59 and 2.81 eV, respectively, indicating that both the catalysts are able to absorb only UV light [35].

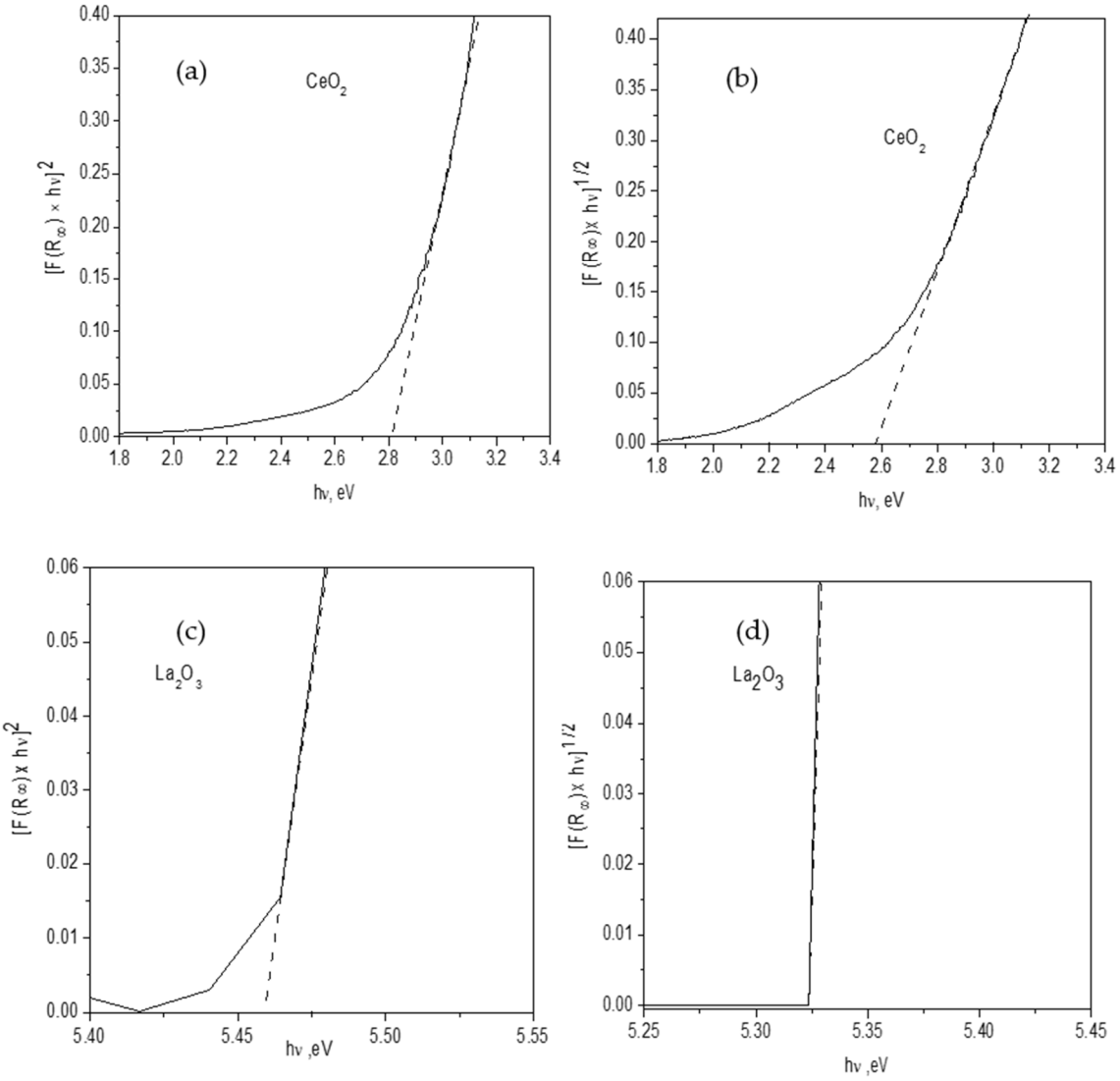

Figure 3. Band gap energy calculation using UV–VIS DRS spectra of CeO_2 and La_2O_3 samples. (**a**) Eg_d evaluation of CeO_2. (**b**) Eg_i evaluation of CeO_2. (**c**) Eg_d evaluation of La_2O_3. (**d**) Eg_i evaluation of La_2O_3.

Raman spectra in the range of 100–1600 cm^{-1} for CeO_2 and La_2O_3 photocatalysts are displayed in Figure 4.

The CeO_2 spectrum exhibited a strong band at about 465 cm^{-1}, corresponding to the symmetrical stretching mode of the Ce-O8 units, typical of CeO_2 with fluorite type structures [36]. It is worthwhile to note the appearance of a red shift of the main peak from 461 cm^{-1} (reported in the Raman spectrum of bulk CeO_2 nanoparticles [37]) to 465 cm^{-1} detected in the CeO_2 Raman spectrum of Figure 4. This effect can be attributed to oxygen vacancies in the CeO_2 lattice leading to defective structures, inducing an enhancement of the photocatalytic activity. The La_2O_3 spectrum evidenced bands located at 101, 192, 407, 1087, 1205, and 1481 cm^{-1}. The most intense Raman signal located at 407 cm^{-1} corresponds to the La–O vibration [38].

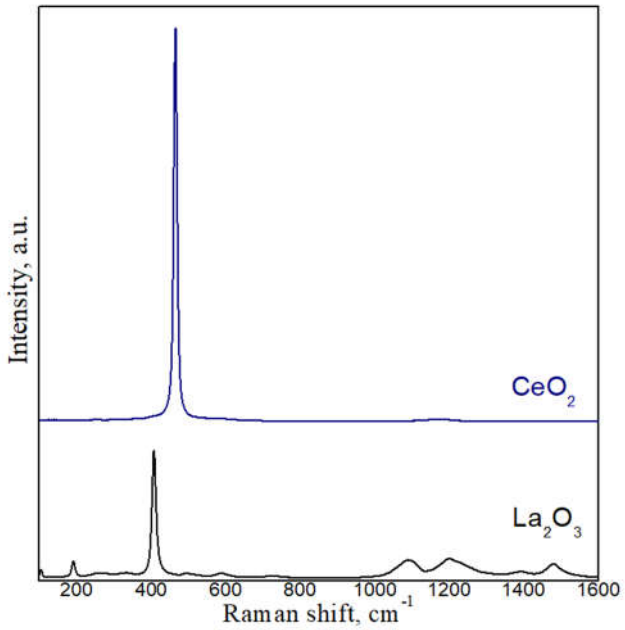

Figure 4. Raman spectra of CeO_2 and La_2O_3 photocatalysts.

The FTIR spectra in the range of 400–4000 cm^{-1} for CeO_2 and La_2O_3 photocatalysts are shown in Figure 5.

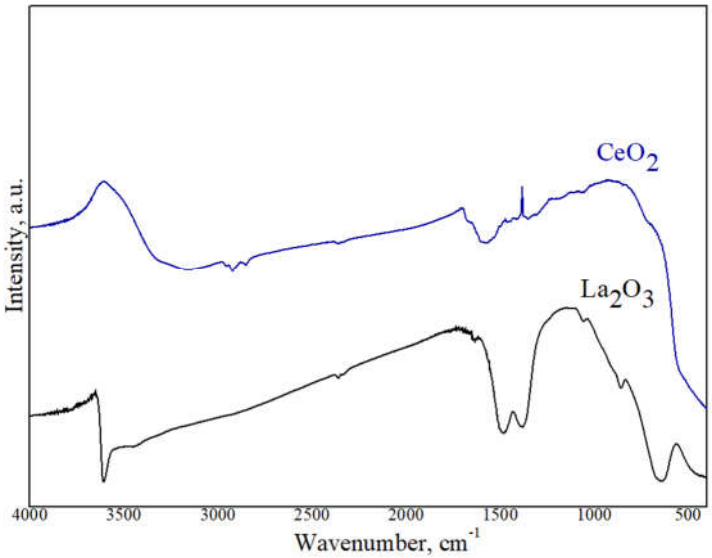

Figure 5. FTIR spectra of CeO_2 and La_2O_3 photocatalysts.

The spectrum of the La_2O_3 photocatalyst shows a band at 645 cm^{-1} associated with the La-O stretching vibration [39]. The bands at about 1462 and 1387 cm^{-1} are linked to COO^- functional groups [28]. Another sharp band sharp band at about 856 cm^{-1} could be associated with associated with C–O bending vibrations [28]. The band observed at about 3600 cm^{-1} evidences the presence of O–H stretching vibrations associated with water adsorbed on the La_2O_3 surface [40]. The spectrum of CeO_2 shows a broad band extending in the range of 3000–3610 cm^{-1} due to the O-H stretching vibration of OH–groups. The signal at around 1579 cm^{-1} is ascribed to the bending vibration of C-H stretching. Moreover, the stretching vibration of the Ce—O bond was observed at about 555 cm^{-1} [30,41,42].

BET plots of La_2O_3 and CeO_2 are shown in Figure S1 in the Supplementary Materials and the obtained S_{BET} are reported in Table 1. It is possible to observe that the S_{BET} of

La_2O_3 (12 m^2 g^{-1}) was significantly higher than of CeO_2 (2.4 m^2 g^{-1}). The pore volume and mean pore radius are reported in Table S1 in the Supplementary Materials. These results were in agreement with S_{BET} values. Indeed, the La_2O_3 pore volume and mean pore radius were higher than CeO_2.

3.2. Levofloxacin Photodegradation Results

Preliminary experiments were carried out under dark conditions to evaluate the possible extent of the adsorption process. Under these conditions, 19% of LEV removal was observed in the presence of CeO_2 (Figure 6A), whereas no removal was observed in the presence of La_2O_3 (Figure 6B).

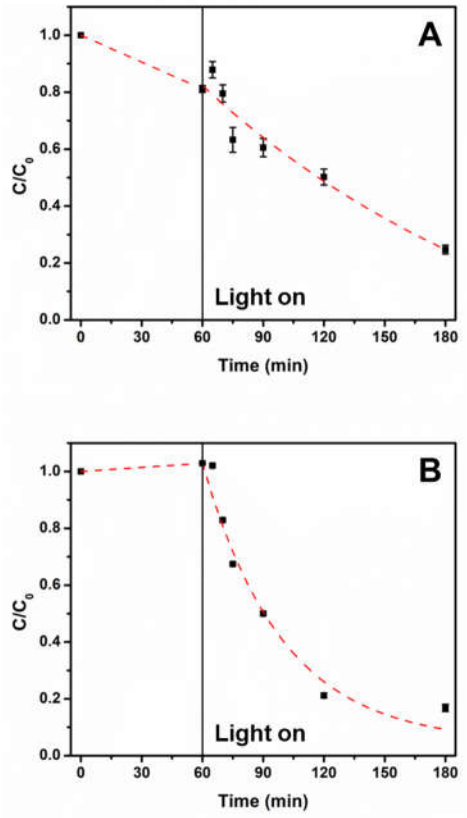

Figure 6. Reduction in LEV as a function of time during photocatalytic treatment at pH 7 in the presence of the catalysts CeO_2 (**A**) and La_2O_3 (**B**). Average results of duplicate measurements are shown.

After the dark step, the SS light was turn on and the photocatalytic process was brought ahead for 120 min with regular sampling at a determined interval time. The collected sample was then analyzed using HPLC-UV showing a gradual decrease in LEV concentration using both CeO_2 and La_2O_3.

In detail, after 120 min of irradiation time, the CeO_2 and La_2O_3 processes allowed us to achieve between 75% and 83% of LEV removal, respectively. The better photocatalytic performance observed in the presence of La_2O_3 can be ascribed to its higher BET surface area and pore volume.

It is worth noting that LEV photodegradation utilizing pure CeO_2 and La_2O_3 was never studied in the literature. Indeed, only papers dealing with the coupling of CeO_2 with other compounds for photocatalytic removal of this drug have been reported [43–46].

3.3. Photocatalytic Inactivation Results

The removal of the levofloxacin-resistant *E. faecalis* ATCC 29212 strain starting from an initial concentration of 1.0×10^6 CFU/mL is shown in Figure 7. Preliminary tests were carried out in dark to assess the natural decay of the target bacteria. No significant effects

could be observed. The CeO_2 system yielded a complete inactivation (2.5 log bacterial decrease) after 60 min. The La_2O_3 system showed a higher degradation rate given that the Enterococci inactivation occurs only after 5 min through a drastic decrease of approximately 2.1 log unit enterococci starting from the dark phase. Similarly, to the tests conducted on the photodegradation of LEV, this analysis on bacterial inactivation showed that the most effective system was the La_2O_3.

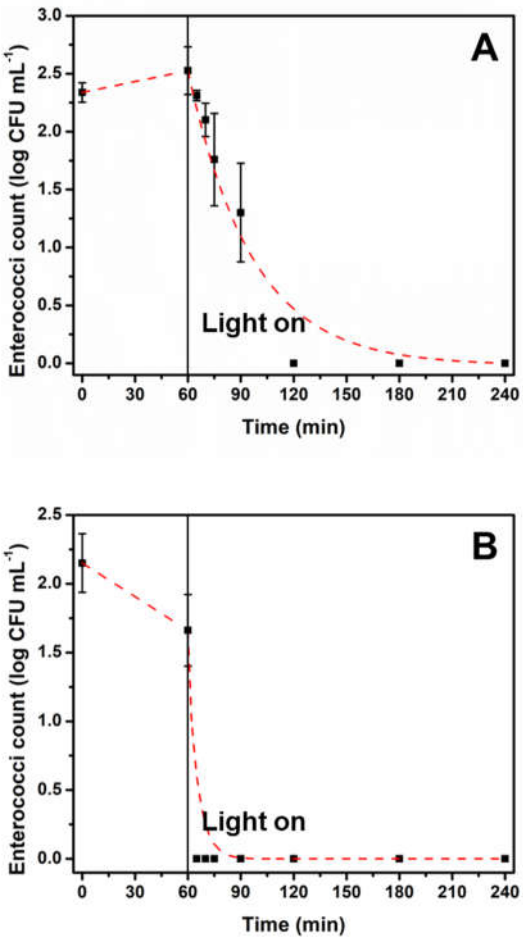

Figure 7. Effect of simulated solar radiation coupled with 0.5 g/L of REE catalysts on the inactivation of levofloxacin-resistant *Enterococcus faecalis* ATCC 29212 strain. (**A**) CeO_2 and (**B**) La_2O_3. Results are shown as the logarithm of CFU mL^{-1}.

Based on these preliminary results, the combination of rare earth elements (REEs) with catalysts in AOPs is a promising treatment for the removal of both chemical and microbiological CECs, due to the exceptional properties of rare earth elements. Moreover, the possibility to use REE-combined catalysts deserve to be investigated in order to further improve the process behaviors.

4. Conclusions

Pure La_2O_3 and CeO_2 photocatalysts were synthesized by using a co-precipitation process, and the physical, chemical, and optical properties were studied with several characterization techniques. WAXD analysis confirmed the crystalline structure for both samples, showing the presence of all diffraction peaks related to the cubic fluorite and hexagonal crystalline structure for CeO_2 and La_2O_3, respectively, while UV–vis DRS spectra showed that both of the samples had a higher absorption contribution in the UV region. This optical feature of the samples was confirmed using Eg_i (2.59 eV) and Eg_d (2.81 eV) values for CeO_2 and Eg_i (5.32 eV) and Eg_d (5.46 eV) values for La_2O_3.

The preliminary study on the degradation of the drug levofloxacin highlights how REE-based catalysts can play an important role in the removal of CECs. After 120 min, the SS/ La_2O_3 process allowed for a removal (83%) higher than the SS/CeO_2 process (75%). Overall, the La_2O_3 system showed the best degradation performance in kinetic terms both with regard to the chemical and biological target. Moreover, the CeO_2 and La_2O_3 processes allowed us to achieve a complete inactivation of *Enterococcus faecalis* ATCC 29212 after 60 min and 5 min, respectively. The use of powder nano-catalysts represents one of the main limitations to full-scale applications of these processes, due to the difficulty to recover the catalysts at the end of the treatment. To overcome this drawback and optimize process behaviors, the immobilization of nanoparticles on macroscopic supports should be attempted.

Supplementary Materials: The following supporting information can be downloaded at: https://www.mdpi.com/article/10.3390/separations11090272/s1, Figure S1: BET plots of (a) La_2O_3 and (b) CeO_2; Table S1: BJH method parameters.

Author Contributions: Conceptualization, G.L. (Giusy Lofrano), V.V., G.L. (Giovanni Libralato) and M.C.; methodology, O.S., A.M., G.L. (Giusy Lofrano) and M.C.; validation, O.S., A.M., G.L. (Giovanni Libralato), M.C. and V.V.; formal analysis, G.L. (Giovanni Libralato), M.C. and G.L. (Giusy Lofrano); investigation, L.S., O.S., A.M. and A.C.; data curation, L.S., A.M., O.S. and A.C.; writing—original draft preparation, L.S., O.S., A.M., G.L. (Giusy Lofrano) and A.C.; writing—review and editing O.S., V.V., A.M., G.L. (Giusy Lofrano) and M.C.; visualization, V.V. and G.L. (Giovanni Libralato). All authors have read and agreed to the published version of the manuscript.

Funding: This work was partially realized in the framework of the project—Removal of emerging halogenated pollutants by advanced oxidation processes: a multiapproach assessment (REHAPOAP)—with the technical and economic support of the Italian Ministero dell'Università e della Ricerca (Investimento 1.1 "Progetti di Ricerca di Rilevante Interesse Nazionale (PRIN PNRR 2022)") (Codice del Progetto: P2022P3ENB). We also acknowledge INPS for funding the PhD of Lorenzo Saviano.

Data Availability Statement: The data presented in this study are available on request from the corresponding authors.

Conflicts of Interest: The authors declare no conflicts of interest.

References

1. Lofrano, G.; Pedrazzani, R.; Libralato, G.; Carotenuto, M. Advanced oxidation processes for antibiotics removal: A review. *Curr. Org. Chem.* **2017**, *21*, 1054–1067. [CrossRef]
2. Szczepanowski, R.; Linke, B.; Krahn, I.; Gartemann, K.H.; Gützkow, T.; Eichler, W.; Pühler, A.; Schlüter, A. Detection of 140 clinically relevant antibiotic-resistance genes in the plasmid metagenome of wastewater treatment plant bacteria showing reduced susceptibility to selected antibiotics. *Microbiology* **2009**, *155*, 2306–2319. [CrossRef] [PubMed]
3. Jyoti, K.; Soni, K.; Chandra, R. Pharmaceutical industrial wastewater exhibiting the co-occurrence of biofilm-forming genes in the multidrug-resistant bacterial community poses a novel environmental threat. *Aquat. Toxicol.* **2024**, *273*, 107019. [CrossRef] [PubMed]
4. Codelia-Anjum, A.; Lerner, L.B.; Elterman, D.; Zorn, K.C.; Bhojani, N.; Chughtai, B. Enterococcal Urinary Tract Infections: A Review of the Pathogenicity, Epidemiology, and Treatment. *Antibiotics* **2023**, *12*, 778. [CrossRef]
5. Collivignarelli, M.C.; Abbà, A.; Benigna, I.; Sorlini, S.; Torretta, V. Overview of the Main Disinfection Processes for Wastewater and Drinking Water Treatment Plants. *Sustainability* **2018**, *10*, 86. [CrossRef]
6. Xue, B.; Guo, X.; Cao, J.; Yang, S.; Qiu, Z.; Wang, J.; Shen, Z. The occurrence, ecological risk, and control of disinfection by-products from intensified wastewater disinfection during the COVID-19 pandemic. *Sci. Total Environ.* **2023**, *900*, 165602. [CrossRef]
7. Fiorentino, A.; Lofrano, G.; Cucciniello, R.; Carotenuto, M.; Motta, O.; Proto, A.; Rizzo, L. Disinfection of roof harvested rainwater inoculated with E. coli and Enterococcus and post-treatment bacterial regrowth: Conventional vs solar driven advanced oxidation processes. *Sci. Total Environ.* **2021**, *801*, 149763. [CrossRef]
8. Aguilar-Ascón, E.; Solari-Godiño, A.; Cueva-Martínez, M.; Neyra-Ascón, W.; Albrecht-Ruíz, M. Characterization of Sludge Resulting from Chemical Coagulation and Electrocoagulation of Pumping Water from Fishmeal Factories. *Processes* **2023**, *11*, 567. [CrossRef]
9. Ahmed, S.A.; Surkatti, R.; Ba-Abbad, M.M.; El-Naas, M.H. Optimization of the Biotreatment of GTL Process Water Using Pseudomonas aeruginosa Immobilized in PVA Hydrogel. *Processes* **2022**, *10*, 2568. [CrossRef]
10. Mishra, S.; Sundaram, B. A review of the photocatalysis process used for wastewater treatment. *Mater. Today Proc.* **2023**, *in press*. [CrossRef]

11. Sarker, T.; Tahmid, I.; Sarker, R.K.; Dey, S.C.; Islam, M.T.; Sarker, M. ZIF-67-based materials as adsorbent for liquid phase adsorption-a review. *Polyhedron* **2024**, *260*, 117069. [CrossRef]
12. Araújo, E.S.; Pereira, M.F.; da Silva, G.M.; Tavares, G.F.; Oliveira, C.Y.; Faia, P.M. A Review on the Use of Metal Oxide-Based Nanocomposites for the Remediation of Organics-Contaminated Water via Photocatalysis: Fundamentals, Bibliometric Study and Recent Advances. *Toxics* **2023**, *11*, 658. [CrossRef] [PubMed]
13. Keerthana, S.P.; Yuvakkumar, R.; Kumar, P.S.; Ravi, G.; Velauthapillai, D. Rare earth metal (Sm) doped zinc ferrite ($ZnFe_{(2)}O_{(4)}$) for improved photocatalytic elimination of toxic dye from aquatic system. *Environ. Res.* **2021**, *197*, 111047. [CrossRef] [PubMed]
14. Vaiano, V.; Matarangolo, M.; Murcia, J.; Rojas, H.; Navío, J.A.; Hidalgo, M. Enhanced photocatalytic removal of phenol from aqueous solutions using ZnO modified with Ag. *Appl. Catal. B Environ.* **2018**, *225*, 197–206. [CrossRef]
15. Kaviyarasu, K.; Matinise, N.; Mayedwa, N.; Mongwaketsi, N.; Letsholathebe, D.; Mola, G.; AbdullahAl-Dhabi, N.; Valan Arasu, M.; Henini, M.; Kennedy, J. Evaluation on La_2O_3 garlanded ceria heterostructured binary metal oxide nanoplates for UV/visible light induced removal of organic dye from urban wastewater. *S. Afr. J. Chem. Eng.* **2018**, *26*, 49–60.
16. Kajjumba, G.W.; Marti, E.J. A review of the application of cerium and lanthanum in phosphorus removal during wastewater treatment: Characteristics, mechanism, and recovery. *Chemosphere* **2022**, *309*, 136462. [CrossRef]
17. Chan, S.H.S.; Yeong Wu, T.; Juan, J.C.; Teh, C.Y. Recent developments of metal oxide semiconductors as photocatalysts in advanced oxidation processes (AOPs) for treatment of dye waste-water. *J. Chem. Technol. Biotechnol.* **2011**, *86*, 1130–1158. [CrossRef]
18. Li, R.; Zhou, Y.; Wang, X.; Wang, L.; Ning, P.; Tao, L.; Cai, J. Removal of elemental mercury by photocatalytic oxidation over La2O3/Bi2O3 composite. *J. Environ. Sci.* **2021**, *102*, 384–397. [CrossRef]
19. Zhang, C.; Ahmad, I.; Ahmed, S.B.; Ali, M.D.; Karim, M.R.; Bayahia, H.; Khasawneh, M.A. A review of rare earth oxides-based photocatalysts: Design strategies and mechanisms. *J. Water Process Eng.* **2024**, *63*, 105548. [CrossRef]
20. Deshmukh, S.M.; Tamboli, M.S.; Shaikh, H.; Babar, S.B.; Hiwarale, D.P.; Thate, A.G.; Shaikh, A.F.; Alam, M.A.; Khetre, S.M.; Bamane, S.R. A Facile Urea-Assisted Thermal Decomposition Process of TiO2 Nanoparticles and Their Photocatalytic Activity. *Coatings* **2021**, *11*, 165. [CrossRef]
21. El-Eskandarany, M.S.; Al-Hazza, A.; Al-Hajji, L.A.; Ali, N.; Al-Duweesh, A.A.; Banyan, M.; Al-Ajmi, F. Mechanical Milling: A Superior Nanotechnological Tool for Fabrication of Nanocrystalline and Nanocomposite Materials. *Nanomaterials* **2021**, *11*, 2484. [CrossRef] [PubMed]
22. Saviano, L.; Brouziotis, A.A.; Suarez, E.G.P.; Siciliano, A.; Spampinato, M.; Guida, M.; Trifuoggi, M.; Del Bianco, D.; Carotenuto, M.; Spica, V.R.; et al. Catalytic Activity of Rare Earth Elements (REEs) in Advanced Oxidation Processes of Wastewater Pollutants: A Review. *Molecules* **2023**, *28*, 6185. [CrossRef] [PubMed]
23. Hassanzadeh-Tabrizi, S.; Taheri-Nassaj, E. Economical synthesis of Al2O3 nanopowder using a precipitation method. *Mater. Lett.* **2009**, *63*, 2274–2276. [CrossRef]
24. Singh, K.; Kumar, K.; Srivastava, S.; Chowdhury, A. Effect of rare-earth doping in CeO2 matrix: Correlations with structure, catalytic and visible light photocatalytic properties. *Ceram. Int.* **2017**, *43*, 17041–17047. [CrossRef]
25. Mirshahghassemi, S.; Lead, J.R. Oil recovery from water under environmentally relevant conditions using magnetic nanoparticles. *Environ. Sci. Technol.* **2015**, *49*, 11729–11736. [CrossRef]
26. Kumar, M.; Rahman, A. Innovations in pn type heterostructure composite materials (La_2O_3/CeO_2) for environmental contamination remediation: Synthesis, characterization, and performance assessment. *Biomass Convers. Biorefinery* **2023**, 1–22. [CrossRef]
27. Kahlmeter, G.; Brown, D.; MacGowan, A.; Goldstein, F.; Mouton, J.; Rodloff, A. EUCAST—The European Committee on Antimicrobial Susceptibility Testing. *Clin. Microbiol. Infect.* **2003**, *9*, 422.
28. Kabir, H.; Nandyala, S.H.; Rahman, M.M.; Kabir, M.A.; Stamboulis, A. Influence of calcination on the sol–gel synthesis of lanthanum oxide nanoparticles. *Appl. Phys. A* **2018**, *124*, 820. [CrossRef]
29. Khalaf, W.M.; Al-Mashhadani, M.H. Synthesis and characterization of lanthanum oxide La_2O_3 net-like nanoparticles by new combustion method. *Biointerface Res. Appl. Chem.* **2022**, *12*, 3066–3075.
30. Farahmandjou, M.; Zarinkamar, M.; Firoozabadi, T. Synthesis of Cerium Oxide (CeO_2) nanoparticles using simple CO-precipitation method. *Rev. Mex. Física* **2016**, *62*, 496–499.
31. Jayakumar, G.; Irudayaraj, A.A.; Raj, A.D. Particle size effect on the properties of cerium oxide (CeO_2) nanoparticles synthesized by hydrothermal method. *Mech. Mater. Sci. Eng. J.* **2017**, *9*, hal-01499374.
32. Prieur, D.; Bonani, W.; Popa, K.; Walter, O.; Kriegsman, K.W.; Engelhard, M.H.; Guo, X.; Eloirdi, R.; Gouder, T.; Beck, A. Size dependence of lattice parameter and electronic structure in CeO_2 nanoparticles. *Inorg. Chem.* **2020**, *59*, 5760–5767. [CrossRef]
33. Madani, R.F.; Sofianty, I.; Sari, A.G.P.; Maryanti, R.; Nandiyanto, A.B.D. Synthesis methods and green synthesis of lanthanum oxide nanoparticles: A review. *Arab. J. Chem. Environ. Res.* **2021**, *8*, 287–314.
34. Mirza, S.H.; Zulfiqar, M.; Azam, S. Effect of hydrostatic pressure on electronic, elastic, and optical properties of hexagonal lanthanum oxide (La_2O_3): A first principles calculations. *Phys. B Condens. Matter* **2024**, *676*, 415686. [CrossRef]
35. Kumar, M.; Rahman, A. Facile synthesis, characterization, and photocatalytic study of La_2O_3/SnO_2 nanocomposites. *J. Inst. Eng. Ser. E* **2023**, *104*, 95–108. [CrossRef]
36. Wheeler, D.; Khan, I. A Raman spectroscopy study of cerium oxide in a cerium–5 wt.% lanthanum alloy. *Vib. Spectrosc.* **2014**, *70*, 200–206. [CrossRef]

37. Su, Z.; Yang, W.; Wang, C.; Xiong, S.; Cao, X.; Peng, Y.; Si, W.; Weng, Y.; Xue, M.; Li, J. Roles of oxygen vacancies in the bulk and surface of CeO2 for toluene catalytic combustion. *Environ. Sci. Technol.* **2020**, *54*, 12684–12692. [CrossRef] [PubMed]
38. Bilel, C.; Jbeli, R.; Ben Jemaa, I.; Dabaki, Y.; Alzaid, M.; Saadallah, F.; Bouaicha, M.; Amlouk, M. Synthesis and physical characterization of Ni-doped La_2O_3 for photocatytic application under sunlight. *J. Mater. Sci. Mater. Electron.* **2021**, *32*, 5415–5426. [CrossRef]
39. Mustofa, K.; Yulizar, Y.; Saefumillah, A.; Apriandanu, D. La_2O_3 nanoparticles formation using *Nothopanax scutellarium* leaf extract in two-phase system and photocatalytic activity under UV light irradiation. *IOP Conf. Ser. Mater. Sci. Eng.* **2020**, *902*, 012018. [CrossRef]
40. Wang, X.; Wang, M.; Song, H.; Ding, B. A simple sol–gel technique for preparing lanthanum oxide nanopowders. *Mater. Lett.* **2006**, *60*, 2261–2265. [CrossRef]
41. Castañeda, C.; Alvarado, I.; Martínez, J.J.; Brijaldo, M.H.; Passos, F.B.; Rojas, H. Enhanced photocatalytic reduction of 4-nitrophenol over Ir/CeO2 photocatalysts under UV irradiation. *J. Chem. Technol. Biotechnol.* **2019**, *94*, 2630–2639. [CrossRef]
42. Culica, M.E.; Chibac-Scutaru, A.L.; Melinte, V.; Coseri, S. Cellulose acetate incorporating organically functionalized CeO_2 NPs: Efficient materials for UV filtering applications. *Materials* **2020**, *13*, 2955. [CrossRef] [PubMed]
43. Wen, X.-J.; Niu, C.-G.; Guo, H.; Zhang, L.; Liang, C.; Zeng, G.-M. Photocatalytic degradation of levofloxacin by ternary Ag2CO3/CeO2/AgBr photocatalyst under visible-light irradiation: Degradation pathways, mineralization ability, and an accelerated interfacial charge transfer process study. *J. Catal.* **2018**, *358*, 211–223. [CrossRef]
44. Ren, Z.; Yang, L.; Tang, X.; Xu, Q.; Niu, Y.; Lv, Y.; Liu, M. Visible light-driven characterisation of AgI/CeO_2/rGO nanocomposites and their application in levofloxacin degradation. *J. Environ. Chem. Eng.* **2024**, *12*, 113124. [CrossRef]
45. Wu, D.; Zhang, X.; Liu, S.; Ren, Z.; Xing, Y.; Jin, X.; Ni, G. Fabrication of a Z-scheme CeO2/Bi2O4 heterojunction photocatalyst with superior visible-light responsive photocatalytic performance. *J. Alloys Compd.* **2022**, *909*, 164671. [CrossRef]
46. Jabbar, Z.H.; Graimed, B.H.; Ammar, S.H.; Al-Jubouri, S.M.; Abbar, A.H.; M-Ridha, M.J.; Taher, A.G. Rational design of novel 0D/0D $Bi_2Sn_2O_7$/CeO_2 in the core-shell nanostructure for boosting the photocatalytic decomposition of antibiotics in wastewater: S-type-based mechanism. *Mater. Sci. Semicond. Process.* **2024**, *173*, 108165. [CrossRef]